Critical investigation of γ-heating rates in stellar matter

Musarat Abbas† Jameel-Un Nabi Arslan Mehmood

University of Wah, Quaid Avenue, Wah Cantt 47040, Punjab, Pakistan

Abstract: The simulation of the observed properties of type I X-ray bursts, also known as superbursts, poses challenges once Cooper pair neutrino emission from the crust of the neutron star are included. Further, additional heating of the accumulating fuel layer is required. The emission of γ-rays caused by electron captures to excited states in astrophysical environments is a major source of heat loss competing with that carried away by weak-interaction neutrinos. γ-heating significantly affect the presupernova evolution of massive stars and the calculation of the thermal structure in the crust and core of superbursts. This energy deposition enhances entropy production and promotes convection at this stage of stellar evolution. Effective γ-heating rates reduce the ignition depth of superbursts. A recent investigation ranked the leading electron capturing nuclei as the cause for significant changes in the lepton-to-baryon fraction (Y_e) of the stellar matter after silicon core burning. We investigate γ-heating rates from the excited states of the top 100 electron capture and positron decay nuclei identified in recently published ranking lists. Each nucleus was analyzed using four different empirical pairing gaps and three distinct sets of nuclear deformation parameters to assess the effect of γ-heating rates. We report our calculations for the temperature range of 1−10 GK and density range of 10^9-10^{11} g/cm^3. The calculated γ-heating rates changes up to a factor 26 (16) with changing deformation values (pairing gaps). Our findings may contribute to more realistic simulations of post-silicon burning phases of massive stars and superbursting neutron stars.

Keywords: γ-heating rates, nuclear deformation, pairing gaps, GT strength distributions, pn-QRPA model

DOI: 10.1088/1674-1137/ae4ba8 **CSTR:** 32044.14.ChinesePhysicsC.50054109

I. INTRODUCTION

The mechanism of energy generation within stars [1], nucleosynthesis [2], and dynamics of supernova explosions [3] continue to be active areas of research in astrophysics. A complete understanding of these phenomena is essential for reliably modeling the evolution of the universe. An earlier study [4] concluded that inefficient core and crust neutrino emissions along with poor crust thermal conductivity are prerequisites for a superbursting neutron star, commonly referred to as superbursts. Superburst ignition column depths were too large because of neutrino cooling attributed to the Cooper pairing of neutrons in the crust. Further, an extra heating mechanism was required in superburst models for simulating observed data. The earliest cooling phases of a neutron star are dominated by neutrino emissions while subsequent cooling is attributed to thermal radiation from the surface. Neutrino cooling reduces the interior temperature of neutron stars to $\geqslant 10^9$ K. For temperatures beyond 10^{10} K, the dominant neutrino emission processes are the modified Urca process and neutrino pair bremsstrahlung in nucleon-nucleon collisions. Flowers *et al*. [5] calculated neutrino emissions in the temperature range of 10^9-10^{10} K for a neutron fluid that has transitioned to the superfluid state. At any nonzero temperature $T < T_c$ (critical temperature), the neutron fluid has two components: a superfluid condensate and quasiparticle excitations. The quasiparticle excitations are induced by broken "Cooper pairs." The authors calculated neutrino pair emissivity because of the recombination of broken pairs that join the condensate, which results in the emission of neutrino-antineutrino pairs. The authors concluded that, in the temperature range of 10^9-10^{10} K, recombination emissivity can dominate all other cooling mechanisms. Superbursts, thought to be a thermonuclear runaway initially caused by carbon unstable burning, possess ignition depths deeper than that of the H/He ignition. Both neutron stars and X-ray bursts are affected by neutrino cooling mechanisms. Superbursts are affected by neutrino losses at a relatively deeper layer inside neutron stars compared to those of usual X-ray bursts [4, 6]. The effects of neutrino cooling on the recurrence time of superbursts depends strongly on thermal neutrino losses (*e.g.*, [6]) for nucleon-

Received 7 November 2025; Accepted 28 February 2026; Accepted manuscript online 1 March 2026

† E-mail: abbaschk87@gmail.com

pair bremsstrahlung and crust Cooper pair breaking and formation process. Gupta *et al*. [6] performed a self-consistent calculation of the thermal structure of superbursts. The authors demonstrated that enabling electron captures to proceed through excited nuclear states led to a significant increase in the thermal energy released within the outer crust of accreting neutron stars. This process offsets the fraction of reaction energy carried away by neutrinos. Although neutrinos freely escape and remove substantial energy from the transparent core at such densities, γ-rays become trapped inside and deposit energy, heating the stellar material. The interplay between neutrino cooling and γ-heating contributes to oxygen deflagration and helps trigger convective motion in the core. Further, they emphasized that the resulting crustal heating is highly sensitive to the initial nuclear composition formed during the burning of lighter elements in the envelope of the neutron star. This sensitivity can be attributed to the strong shell and subshell effects in neutron-rich nuclei, triggering notable changes in nuclear shape, single-particle structure, and electron-capture strength distributions even for nuclei with comparable proton and mass numbers. Gupta *et al.* computed γ-heating rates that were bigger by a factor of 10 at densities $\leq 10^{11}$ g/cm^3 than that estimated previously. These higher γ-heating rates shortened the ignition column depths counteracting the effect of reduction in temperature from the Cooper pairing of neutrons in the crust. The higher calculated γ-heating rates supported the reduction in the discrepancy between temperatures required for unstable ^{12}C ignition on timescales consistent with the observations. Crustal heating calculations were very sensitive to the underlying nuclear physics. The authors stressed on a reliable calculation of the nuclear structure and β-decay properties of very neutron-rich nuclei up to a mass number of 106. Such a calculation can constrain the lowest lying electron capture strength, which in turn determines the γ-heating rates.

During the final life cycle stages of a massive star, weak-interaction processes are significantly influenced by charge-exchange mechanisms, which are also referred to as Gamow-Teller (GT) transitions [7]. These reactions, governed by the weak force, subsequently affect γ-heating and neutrino cooling rates. Key processes in stellar core collapse, including magnetorotational instabilities [8], electron capture (EC) on nuclei, and resulting γ-heating are highly temperature-dependent. As the collapse proceeds, the stellar core is compressed to nuclear densities, after which it rebounds against stiff nuclear matter. This rebound drives the ejection of parts of the heavy-element core along with outer shells into the interstellar medium [9]. At this stage, γ-heating may assist in re-energizing the stalled shock, supporting explosive burning and driving convection. In the late evolutionary stages of massive stars, weak interaction processes play a decisive role in regulating the energy balance of the core.

Nuclear shapes and pairing gaps are two crucial parameters used to investigate various nuclear structure properties including those possessing astrophysical significance. Experimental studies of atomic nuclei have revealed that they can adopt various spherical or ellipsoidal shapes. In many cases, the ellipsoidal configurations exhibit significant deviations from the ideal spherical configuration referred to as deformations. Such nuclear deformations are prominent in nuclei far from magic numbers associated with enhanced stability. As nuclei moves away from the stability line, weaker nucleon binding and greater imbalance between protons and neutrons result in substantial alterations to the nuclear potential. The spin–isospin component of the nucleon–nucleon interaction influences these effects by modifying single-particle energy levels. The growing importance of many-body correlations amplify these effects, which results in the breakdown of conventional shell closures and emergence of new ones. The evolution of nuclear shapes across different regions of the nuclear chart remains an active area of research, investigated through a wide range of experimental [10, 11] and theoretical approaches [12−14]. Meanwhile, a better understanding of the nucleon pairing effect in nuclear matter is pivotal for interpreting a spectrum of astrophysical phenomena associated with compact stellar objects. These include the thermal evolution of nascent neutron stars [15], post-outburst relaxation dynamics in X-ray bursts [16], and pulsar glitch dynamics [17, 18].

A robust theoretical characterization of pairing correlations necessitates incorporating precise bare nucleon-nucleon interactions. However, the magnitude and behavior of pairing gaps within nuclear matter remain constrained [19], posing a significant challenge to predictive modeling efforts.

Several theoretical studies have investigated the effect of temperature on nuclear properties (*e.g.*, [20−32]. The pairing of nucleons was neglected in the calculations for hot giant dipole resonance (GDR) because it was believed that the gap vanishes at $T = T_c < 1$ MeV according to the BCS theory. Subsequently, it was discovered that thermal fluctuations smear out the superfluid-normal phase transition in finite systems so that the pairing gap survives up to $T \gg 1$ MeV [28]. The effect of thermal pairing causes a smaller GDR width at $T \leq 2$ MeV compared to the one obtained by neglecting pairing [24]. Other approaches support the argument that pairing correlations do not abruptly disappear at $T \neq 0$ [29−31]. Ref. [33] suggests that the decrease in the pairing gap with increasing temperature, which is also caused by particle-particle and hole-hole configurations at low temperatures, can slow down the increase in GDR width. An investigation conducted to study the temperature dependence of the pairing gap beyond the BCS approximation led to no-

ticeably higher values of the critical temperature [26]. The equation of motion for the two-fermion two-time correlation function in the pairing channel was considered at finite temperature for ^{68}Ni, ^{44}Ca, and ^{46}Ca. It was concluded that, in the pure BCS case, the pairing gap decreased quickly with the increase in temperature and disappeared around T= 1.2 MeV. However, in the BCS + particle-vibration coupling calculation, the gap values were still significant around T= 1 MeV. The pairing gap retained its peaked character in the BCS + particle-vibration coupling calculation even when its average value decreased with a rise in temperature. Authors explored the nuclear shell structure of nickel isotopes in a finite-temperature relativistic framework [27]. In these calculations, pairing correlations were considered up to temperatures of 1 MeV.

One of the noticeable works related to the finite temperature investigation of nuclear properties was reported by Ravlić *et al.* [32]. The authors presented the mapping of nuclear drip lines at temperatures up to T =20 GK using the relativistic energy density functional theory, including the treatment of the thermal scattering of nucleons in the continuum. The authors did not incorporate approaches beyond the mean field nor account for statistical (thermal) fluctuations in their calculations. These findings stated that the pairing gaps and deformation properties were present at least up to T= 10 GK ($\sim$ 1 MeV). They commented that for temperatures beyond 1 MeV, these two nuclear structure properties may still exist provided thermal fluctuations are considered. Furthermore, the authors reported that, for $T \leq$ 12 GK, the interplay between the properties of nuclear effective interaction, pairing, and temperature effects determine the nuclear binding. At higher temperatures, the pairing correlations disappear, shell effects vanish, and a transition occurs from the superfluid to the normal state. The authors commented that nuclear deformation decreased with temperature, which leads to a transition from the deformed to the spherical state. At T = 1 MeV, the authors found a significant number of nuclei exhibiting deformation effects. It may be safely concluded from the above arguments that pairing and deformation effects exist at least up to T= 10 GK. Consequently, we present our calculations on the effects of pairing gaps and nuclear deformation on γ-heating rates only up to T= 10 GK ($\sim$ 1 MeV).

We used the proton-neutron quasiparticle random phase approximation (pn-QRPA) model [34] to calculate γ-heating rates in stellar environment. Our nuclear model did not consider the smearing of the Fermi surface because of heating effects. However, we consider the smearing of the nuclear Fermi-surface because of pairing correlation in our current calculation. There are studies based on quasiparticle randomphase approximation (QRPA) formalism that include the effect of finite temperature in the calculation of nuclear matrix elements (NMEs) of Fermi and GT transitions. The studies performed by Dzhioev *et al.* [35] were based on the TQRPA approach in which temperature is considered within the thermo-field dynamics formalism using the Woods-Saxon potential, BCS pairing interactions, and separable multipole and spin-multipole particle-hole interactions. TQRPA enables determining temperature-dependent spectral functions and treats the ground state and thermally excited states consistently on the level of 2p-2h correlations. A self-consistent FTQRPA approach within relativistic [36] and non-relativistic [37] frameworks, based on nuclear energy density functionals for evaluating nuclear weak interaction rates, is available at finite temperature. The evolution of the GT$_+$ spectrum with temperature was investigated using the finite-temperature proton-neutron relativistic time blocking approximation and finite-temperature proton-neutron relativistic random phase approximation models [38]. The calculations showed only minor changes in the GT$_+$ distributions for the nuclei around ^{78}Ni when the temperature increased from 0 to around 1 MeV [38]. The relativistic and nonrelativistic finite temperature proton-neutron quasiparticle random phase approximation methods were developed to study the interplay of the pairing and temperature effects on the GT excitations in open-shell nuclei [39]. The findings showed that pairing effects are crucial for a proper description of the spin-isospin excitations, especially at temperatures below 1 MeV and further concluded that the thermal evolution of the GT$_-$ spectrum for ^{42}Ca, ^{46}Ti, and ^{118}Sn displayed small changes up to temperatures of 1 MeV. Our model has an advantage which makes our calculation of reduced transition probabilities more reliable than other nuclear models. Our model is perhaps one of the very few models that calculate GT strength distributions from the parent ground and low-lying excited states (up to 10 MeV) in a microscopic fashion. Other models (*e.g.*, [40−45]) calculate the GT distributions from the ground state (and perhaps a few low-lying states up to 1−2 MeV) and the remaining parent levels assume the Brink-Axel hypothesis [46, 47]. The Brink-Axel hypothesis is not a good approximation for estimating excited state GT distribution functions [48].

Based on a simulation study of presupernova evolution, Nabi *et al.* [49] identified a suite of crucial electron capture nuclei whose reaction rates most significantly influenced the dynamics of stellar core collapse. The authors selected an ensemble consisting of 728 nuclei with a mass range of A = 1−100 and adopted a novel recipe for computing nuclear partition functions. The capture rates on these nuclei directly govern the lepton fraction rate of the core ($\dot{Y}_e$) and entropy, which plays a fundamental role in the initial collapse dynamics and subsequent supernova mechanism. The authors published an updated list of electron capturing nuclei, which had the largest effect on $\dot{Y}_e$ for conditions after silicon core burning. We selec-

ted the top 100 electron capturing nuclei for the current investigation of γ-heating rates.

The γ-heating rates for the top 100 EC nuclei were calculated using four different pairing-gap prescriptions: (i) Lipkin–Nogami ($\Delta^{(LN)}$) [50], (ii) Madland–Nix ($\Delta^{(MN)}$) [51], (iii) four-point ($\Delta^{(4)}$) [52], and five-point ($\Delta^{(5)}$) [52] empirical pairing models. In addition, three sets of nuclear deformation parameters, which correspond to β_2 values from the FRLDM (1981) [53], FRDM (1992) [54], and FRDM (2012) [55] models, were employed as input parameters in our nuclear model for investigating their effects on computed γ-heating rates.

This paper is organized as follows: Section II outlines the theoretical framework for the calculation of γ-ray heating energy rates. Section III presents and discusses calculated results in depth and presents a comparison with the available measured data. Finally, Section IV provides a concise summary of the main conclusions and implications of the present investigation.

II. FORMALISM

This study aims to investigate the effects of nuclear shape and nucleon pairing gaps on the computed γ-heating rates. The charge-changing transitions were calculated using the pn-QRPA model with a simple pairing plus quadrupole Hamiltonian with the incorporation of particle-particle (pp) and particle-hole (ph) GT forces of the separable form. We began with a spherical single-particle basis ($s^{\dagger}_{jm}$, s_{jm}) and introduced an axially symmetric deformation that generated the corresponding canonical (Nilsson) basis ($D^{\dagger}_{m\alpha}$, $D_{m\alpha}$).

$$D^{\dagger}_{m\alpha} = \sum_{j} T^{m}_{j\alpha}\, s^{\dagger}_{jm}, \tag{1}$$

where m represents the projection of angular momentum onto the symmetry axis, while α represents additional quantum numbers to determine the states completely. The transformation matrix T includes Nilsson eigenfunctions within the Nilsson+BCS model. The quasiparticle (Q) basis was defined using yet another transformation, expressed as

$$Q^{\dagger}_{m\alpha} = u_{m\alpha} D^{\dagger}_{m\alpha} - v_{m\alpha} D_{\bar{m}\alpha}, \tag{2}$$

$$Q^{\dagger}_{\bar{m}\alpha} = u_{m\alpha} D^{\dagger}_{\bar{m}\alpha} + v_{m\alpha} D_{m\alpha}, \quad (m > 0), \tag{3}$$

where $\bar{m}$ represents the time reversed state of m. The occupation amplitude satisfies the condition $u^2_{m\alpha} = v^2_{m\alpha} = 1$. We employed the BCS theory to determine the values of u and v. The pn-QRPA phonons creation operators $\hat{\Phi}$ were expressed as

$$\hat{\Phi}^{\dagger}_{\Psi}(\mu) = \sum_{pn} X^{pn}_{\Psi}(\mu)\hat{Q}^{\dagger}_{p}\hat{Q}^{\dagger}_{\bar{n}} - Y^{pn}_{\Psi}(\mu)\hat{Q}_{n}\hat{Q}_{\bar{p}}\,, \tag{4}$$

The indices n and p distinguished between the single quasi-particle states of the neutron and proton, and they represent $m_p\alpha_p$ and $m_n\alpha_n$, respectively. The sum fulfilled the conditions $\mu = m_p - m_n = 0, \pm 1$ and $\pi_p.\pi_n = 1$ for the neutrons and protons pairs. The term Ψ represents the energy eigenvalues, while forward- and backward-amplitudes (X) and (Y) are the eigenfunctions of the RPA equation for proton-neutron quasiparticle pair states

$$\begin{bmatrix} M & N \\ -N & -M \end{bmatrix} \begin{bmatrix} X \\ Y \end{bmatrix} = \Psi \begin{bmatrix} X \\ Y \end{bmatrix}. \tag{5}$$

The RPA equations were solved separately for each values of μ. The details of the elements of submatrices M and N have been reported in Ref. [56].

A. Extension to odd-odd and odd-A mass nuclei

The RPA framework was initially employed to calculate excitation states from the ground state of even–even nuclei. Subsequently, the authors in Ref. [56] extended the model to odd–odd and odd-A systems. For odd-A nuclei, two types of transitions are possible. The first corresponds to a phonon excitation in which the odd particle does not take part in the interaction, while the second type involves transition between one-quasiparticle states. Phonon correlations were incorporated in one-quasiparticle configurations using the first-order perturbation theory

$$|p_{corr}\rangle = Q^{\dagger}_{p}|-\rangle + \sum_{n,\Psi} Q^{\dagger}_{n}\hat{\Phi}^{\dagger}_{\Psi}(\mu)|-\rangle \times \langle -|[Q^{\dagger}_{n}\hat{\Phi}^{\dagger}_{\Psi}(\mu)]^{\dagger} H_{31} Q^{\dagger}_{p}|-\rangle \times E_{p}(n,\Psi), \tag{6}$$

$$|n_{corr}\rangle = Q^{\dagger}_{n}|-\rangle + \sum_{p,\Psi} Q^{\dagger}_{p}\hat{\Phi}^{\dagger}_{\Psi}(-\mu)|-\rangle \times \langle -|[Q^{\dagger}_{p}\hat{\Phi}^{\dagger}_{\Psi}(-\mu)]^{\dagger} H_{31} Q^{\dagger}_{n}|-\rangle \times E_{n}(p,\Psi), \tag{7}$$

$$E_{i}(j,\Psi) = \frac{1}{\epsilon_{i} - \epsilon_{j} - \Psi}, \quad (i,j = p,n), \tag{8}$$

where ϵ represents quasi-particle energies. The quasi-particle-phonon coupled Hamiltonian term H_{31} in Eqs. (6) and (7) was defined using

$$
\begin{aligned}
H_{31} = & \sum V_{pn,\bar{p'n'}}(u_p u_n v_{p'} u_{n'} - v_p v_n u_{p'} v_{n'}) \\
& \times (Q_p^\dagger Q_n^\dagger Q_{p'}^\dagger Q_{n'} + h.c.) \\
& + \sum V_{pn,\bar{p'n'}}(v_p v_n v_{p'} u_{n'} - u_p u_n u_{p'} v_{n'}) \\
& \times (Q_p^\dagger Q_n^\dagger Q_{n'}^\dagger Q_{p'} + h.c.) \,, \qquad (9)
\end{aligned}
$$

where the Hermitian conjugate ($h.c$) terms ensure the proper symmetry of the operators. V represents the two-body interaction matrix elements. The explicit form of V for a separable and schematic interaction as well as charge-changing transition amplitudes between correlated one-quasiparticle states have been reported in Ref. [56]. The idea of quasiparticle transitions with first-order phonon correlations can be extended to an odd-odd parent nucleus. The ground state is assumed to be a proton–neutron quasiparticle pair state of the smallest energy. The GT transitions of the quasiparticle lead to two-proton or two-neutron quasiparticle states in the daughter nucleus. The two-quasiparticle states were constructed with phonon correlations and given by

$$
\begin{aligned}
|pn_{corr}> = & Q_p^\dagger Q_n^\dagger|-> + \frac{1}{2}\sum_{p'_1,p'_2,\Psi} Q_{p'_1}^\dagger Q_{p'_2}^\dagger \hat{\Phi}_\Psi^\dagger(-\mu)|-> \times < -|[Q_{p'_1}^\dagger Q_{p'_2}^\dagger \hat{\Phi}_\Psi^\dagger(-\mu)]^\dagger H_{31} Q_p^\dagger Q_n^\dagger|-> E_{pn}(p'_1 p'_2, \Psi) \\
& + \frac{1}{2}\sum_{n'_1,n'_2,\Psi} Q_{n'_1}^\dagger Q_{n'_2} \hat{\Phi}_\Psi^\dagger(\mu)|-> \times < -|[Q_{n'_1}^\dagger Q_{n'_2}^\dagger \hat{\Phi}_\Psi^\dagger(\mu)]^\dagger H_{31} Q_p^\dagger Q_n^\dagger|-> E_{pn}(n'_1 n'_2, \Psi) \,, \qquad (10)
\end{aligned}
$$

$$
< p_1 p_{2corr}| = Q_{p_1}^\dagger Q_{p_2}^\dagger|-> + \sum_{p',n',\Psi} Q_{p'}^\dagger Q_{n'}^\dagger \hat{\Phi}_\Psi^\dagger(\mu)|-> \times < -|[Q_{p'}^\dagger Q_{n'}^\dagger \hat{\Phi}_\Psi^\dagger(\mu)]^\dagger H_{31} Q_{p_1}^\dagger Q_{p_2}^\dagger|-> E_{p_1 p_2}(p'n', \Psi) \,, \qquad (11)
$$

$$
< n_1 n_{2corr}| = Q_{n_1}^\dagger Q_{n_2}^\dagger|-> + \sum_{p',n',\Psi} Q_{p'}^+ Q_{n'}^\dagger \hat{\Phi}_\Psi^\dagger(-\mu)|-> \times < -|[Q_{p'}^\dagger Q_{n'}^\dagger \hat{\Phi}_\Psi^\dagger(-\mu)]^\dagger H_{31} Q_{n_1}^\dagger Q_{n_2}^\dagger|-> E_{n_1 n_2}(p'n', \Psi) \,, \qquad (12)
$$

where

$$
E_{ab}(cd, \Psi) = \frac{1}{(\epsilon_a + \epsilon_b) - (\epsilon_c + \epsilon_d + \Psi)}. \qquad (13)
$$

These two-quasiparticle states were expressed in terms of one-quasiparticle transition amplitudes using

$$
\begin{aligned}
& < p_1 p_{2corr}|\tau_\pm \sigma_\mu|pn_{corr}> \\
= & \, \delta(p_1, p) < p_{2corr}|\tau_\pm \sigma_\mu|n_{corr}> \\
& - \delta(p_2, p) < p_{1corr}|\tau_\pm \sigma_\mu|n_{corr}> \,, \qquad (14)
\end{aligned}
$$

$$
\begin{aligned}
& < n_1 n_{2corr}|\tau_\pm \sigma_{-\mu}|pn_{corr}> \\
= & \, \delta(n_2, n) < n_{1corr}|\tau_\pm \sigma_{-\mu}|p_{corr}> \\
& - \delta(n_1, n) < n_{2corr}|\tau_\pm \sigma_{-\mu}|p_{corr}> \,. \qquad (15)
\end{aligned}
$$

When a nucleus contains an odd nucleon, the low-lying excited states are generated by promoting the quasiparticle from the lowest-energy orbital to higher-lying orbitals. For odd-proton even-neutron nuclei, these excited states can be described as three-proton configurations or as one-proton–two-neutron configurations, corresponding to the excitations of a proton or a neutron, respectively,

$$
\begin{aligned}
|p_1 p_2 p_{3corr}\rangle = & Q_{p_1}^\dagger Q_{p_2}^\dagger Q_{p_3}^\dagger|-\rangle + \frac{1}{2}\sum_{p'_1,p'_2,n',\Psi} Q_{p'_1}^\dagger Q_{p'_2}^\dagger Q_{n'}^\dagger \hat{\Phi}_\Psi^\dagger(\mu)|-\rangle \\
& \times \langle -|[Q_{p'_1}^\dagger Q_{p'_2}^\dagger Q_{n'}^\dagger \hat{\Phi}_\Psi^\dagger(\mu)]^\dagger H_{31} Q_{p_1}^\dagger Q_{p_2}^\dagger Q_{p_3}^\dagger|-\rangle E_{p_1 p_2 p_3}(p'_1 p'_2 n', \Psi) \,, \qquad (16)
\end{aligned}
$$

$$
|p_1 n_1 n_{2corr}\rangle = Q_{p_1}^\dagger Q_{n_1}^\dagger Q_{n_2}^\dagger|-\rangle + \frac{1}{2}\sum_{p'_1,p'_2,n',\Psi} Q_{p'_1}^\dagger Q_{p'_2}^\dagger Q_{n'}^\dagger \hat{\Phi}_\Psi^\dagger(-\mu)|-\rangle \times \langle -|[Q_{p'_1}^\dagger Q_{p'_2}^\dagger Q_{n'}^\dagger \hat{\Phi}_\Psi^\dagger(-\mu)]^\dagger H_{31} Q_{p_1}^\dagger Q_{n_1}^\dagger Q_{n_2}^\dagger|-\rangle
$$

$$\times E_{p_1n_1n_2}(p'_1p'_2n',\Psi)+\frac{1}{6}\sum_{n'_1,n'_2,n'_3,\Psi}Q^{\dagger}_{n'_1}Q^{\dagger}_{n'_2}Q^{\dagger}_{n'_3}\hat{\Phi}^{\dagger}_{\Psi}(\mu)|-\rangle\times\langle-|[Q^{\dagger}_{n'_1}Q^{\dagger}_{n'_2}Q^{\dagger}_{n'_3}\hat{\Phi}^{\dagger}_{\Psi}(\mu)]^{\dagger}H_{31}Q^{\dagger}_{p_1}Q^{\dagger}_{n_1}Q^{\dagger}_{n_2}|-\rangle E_{p_1n_1n_2}(n'_1n'_2n'_3,\Psi)\,, \tag{17}$$

with the energy denominators of the first order perturbation

$$E_{abc}(def,\Psi)=\frac{1}{(\epsilon_a+\epsilon_b+\epsilon_c-\epsilon_d-\epsilon_e-\epsilon_f-\Psi)}\,. \tag{18}$$

The transition amplitudes between three–quasiparticle states were reduced to effective amplitudes for correlated one–quasiparticle states

$$\begin{aligned}&\langle p'_1p'_2n'_{1corr}|\tau_{\pm}\sigma_{-\mu}|p_1p_2p_{3corr}\rangle\\&=\delta(p'_1,p_2)\delta(p'_2,p_3)\langle n'_{1corr}|\tau_{\pm}\sigma_{-\mu}|p_{1corr}\rangle\\&\quad-\delta(p'_1,p_1)\delta(p'_2,p_3)\langle n'_{1corr}|\tau_{\pm}\sigma_{-\mu}|p_{2corr}\rangle\\&\quad+\delta(p'_1,p_1)\delta(p'_2,p_2)\langle n'_{1corr}|\tau_{\pm}\sigma_{-\mu}|p_{3corr}\rangle\,,\end{aligned} \tag{19}$$

$$\begin{aligned}&\langle p'_1p'_2n'_{1corr}|\tau_{\pm}\sigma_{\mu}|p_1n_1n_{2corr}\rangle\\&=\delta(n'_1,n_2)[\delta(p'_1,p_1)\langle p'_{2corr}|\tau_{\pm}\sigma_{\mu}|n_{1corr}\rangle\\&\quad-\delta(p'_2,p_1)\langle p'_{1corr}|\tau_{\pm}\sigma_{\mu}|n_{1corr}\rangle]\\&\quad-\delta(n'_1,n_1)[\delta(p'_1,p_1)\langle p'_{2corr}|\tau_{\pm}\sigma_{\mu}|n_{2corr}\rangle\\&\quad-\delta(p'_2,p_1)\langle p'_{1corr}|\tau_{\pm}\sigma_{\mu}|n_{2corr}\rangle]\,,\end{aligned} \tag{20}$$

$$\begin{aligned}&\langle n'_1n'_2n'_{3corr}|\tau_{\pm}\sigma_{-\mu}|p_1n_1n_{2corr}\rangle\\&=\delta(n'_2,n_1)\delta(n'_3,n_2)\langle n'_{1corr}|\tau_{\pm}\sigma_{-\mu}|p_{1corr}\rangle\\&\quad-\delta(n'_1,n_1)\delta(n'_3,n_2)\langle n'_{2corr}|\tau_{\pm}\sigma_{-\mu}|p_{1corr}\rangle\\&\quad+\delta(n'_1,n_1)\delta(n'_2,n_2)\langle n'_{3corr}|\tau_{\pm}\sigma_{-\mu}|p_{1corr}\rangle\,,\end{aligned} \tag{21}$$

and for parent nuclei with an odd neutron

$$\begin{aligned}&\langle p'_1n'_1n'_{2corr}|\tau_{\pm}\sigma_{\mu}|n_1n_2n_{3corr}\rangle\\&=\delta(n'_1,n_2)\delta(n'_2,n_3)\langle p'_{1corr}|\tau_{\pm}\sigma_{\mu}|n_{1corr}\rangle\\&\quad-\delta(n'_1,n_1)\delta(n'_2,n_3)\langle p'_{1corr}|\tau_{\pm}\sigma_{\mu}|n_{2corr}\rangle\\&\quad+\delta(n'_1,n_1)\delta(n'_2,n_2)\langle p'_{1corr}|\tau_{\pm}\sigma_{\mu}|n_{3corr}\rangle\,,\end{aligned} \tag{22}$$

$$\begin{aligned}&\langle p'_1n'_1n'_{2corr}|\tau_{\pm}\sigma_{-\mu}|p_1p_2n_{1corr}\rangle\\&=\delta(p'_1,p_2)[\delta(n'_1,n_1)\langle n'_{2corr}|\tau_{\pm}\sigma_{-\mu}|p_{1corr}\rangle\\&\quad-\delta(n'_2,n_1)\langle n'_{1corr}|\tau_{\pm}\sigma_{-\mu}|p_{1corr}\rangle]\\&\quad-\delta(p'_1,p_1)[\delta(n'_1,n_1)\langle n'_{2corr}|\tau_{\pm}\sigma_{-\mu}|p_{2corr}\rangle\\&\quad-\delta(n'_2,n_1)\langle n'_{1corr}|\tau_{\pm}\sigma_{-\mu}|p_{2corr}\rangle]\quad,\end{aligned} \tag{23}$$

$$\begin{aligned}&\langle p'_1p'_2p'_{3corr}|\tau_{\pm}\sigma_{\mu}|p_1p_2n_{1corr}\rangle\\&=\delta(p'_2,p_1)\delta(p'_3,p_2)\langle p'_{1corr}|\tau_{\pm}\sigma_{\mu}|n_{1corr}\rangle\\&\quad-\delta(p'_1,p_1)\delta(p'_3,p_2)\langle p'_{2corr}|\tau_{\pm}\sigma_{\mu}|n_{1corr}\rangle\\&\quad+\delta(p'_1,p_1)\delta(p'_2,p_2)\langle p'_{3corr}|\tau_{\pm}\sigma_{\mu}|n_{1corr}\rangle\,.\end{aligned} \tag{24}$$

In odd–odd nuclei, low-lying excited states can be described within the quasiparticle framework as either proton–neutron pair configurations or as four–quasiparticle states formed by adding two protons or two neutrons. Although transitions from two–quasiparticle states are treated separately, phonon-correlated four–quasiparticle states can be constructed in an analogous way to two– and three–quasiparticle configurations

$$\begin{aligned}&<p'_1p'_2n'_1n'_{2corr}|\tau_{\pm}\sigma_{-\mu}|p_1p_2p_3n_{1corr}>\\&=\delta(n'_2,n_1)[\delta(p'_1,p_2)\delta(p'_2,p_3)<n'_{1corr}|\tau_{\pm}\sigma_{-\mu}|p_{1corr}>\\&\quad-\delta(p'_1,p_1)\delta(p'_2,p_3)<n'_{1corr}|\tau_{\pm}\sigma_{-\mu}|p_{2corr}>\\&\quad+\delta(p'_1,p_1)\delta(p'_2,p_2)<n'_{1corr}|\tau_{\pm}\sigma_{-\mu}|p_{3corr}>]\\&\quad-\delta(n'_1,n_1)[\delta(p'_1,p_2)\delta(p'_2,p_3)<n'_{2corr}|\tau_{\pm}\sigma_{-\mu}|p_{1corr}>\\&\quad-\delta(p'_1,p_1)\delta(p'_2,p_3)<n'_{2corr}|\tau_{\pm}\sigma_{-\mu}|p_{2corr}>\\&\quad+\delta(p'_1,p_1)\delta(p'_2,p_2)<n'_{2corr}|\tau_{\pm}\sigma_{-\mu}|p_{3corr}>]\,,\end{aligned} \tag{25}$$

$$\begin{aligned}&<p'_1p'_2p'_3p'_{4corr}|\tau_{\pm}\sigma_{\mu}|p_1p_2p_3n_{1corr}>\\&=-\delta(p'_2,p_1)\delta(p'_3,p_2)\delta(p'_4,p_3)<p'_{1corr}|\tau_{\pm}\sigma_{\mu}|n_{1corr}>\\&\quad+\delta(p'_1,p_1)\delta(p'_3,p_2)\delta(p'_4,p_3)<p'_{2corr}|\tau_{\pm}\sigma_{\mu}|n_{1corr}>\\&\quad-\delta(p'_1,p_1)\delta(p'_2,p_2)\delta(p'_4,p_3)<p'_{3corr}|\tau_{\pm}\sigma_{\mu}|n_{1corr}>\\&\quad+\delta(p'_1,p_1)\delta(p'_2,p_2)\delta(p'_3,p_3)<p'_{4corr}|\tau_{\pm}\sigma_{\mu}|n_{1corr}>\,,\end{aligned} \tag{26}$$

$$\begin{aligned}&<p'_1p'_2n'_1n'_{2corr}|\tau_{\pm}\sigma_{\mu}|p_1n_1n_2n_{3corr}>\\&=\delta(p'_1,p_1)[\delta(n'_1,n_2)\delta(n'_2,n_3)<p'_{2corr}|\tau_{\pm}\sigma_{\mu}|n_{1corr}>\\&\quad-\delta(n'_1,n_1)\delta(n'_2,n_3)<p'_{2corr}|\tau_{\pm}\sigma_{\mu}|n_{2corr}>\\&\quad+\delta(n'_1,n_1)\delta(n'_2,n_2)<p'_{2corr}|\tau_{\pm}\sigma_{\mu}|n_{3corr}>]\\&\quad-\delta(p'_2,p_1)[\delta(n'_1,n_2)\delta(n'_2,n_3)<p'_{1corr}|\tau_{\pm}\sigma_{\mu}|n_{1corr}>\\&\quad-\delta(n'_1,n_1)\delta(n'_2,n_3)<p'_{1corr}|\tau_{\pm}\sigma_{\mu}|n_{2corr}>\\&\quad+\delta(n'_1,n_1)\delta(n'_2,n_2)<p'_{1corr}|\tau_{\pm}\sigma_{\mu}|n_{3corr}>]\,,\end{aligned} \tag{27}$$

$$
\begin{aligned}
&< n'_1 n'_2 n'_3 n'_{4corr} | \tau_{\pm} \sigma_{-\mu} | p_1 n_1 n_2 n_{3corr} > \\
= &+ \delta(n'_2, n_1)\delta(n'_3, n_2)\delta(n'_4, n_3) < n'_{1corr} | \tau_{\pm} \sigma_{-\mu} | p_{1corr} > \\
&- \delta(n'_1, n_1)\delta(n'_3, n_2)\delta(n'_4, n_3) < n'_{2corr} | \tau_{\pm} \sigma_{-\mu} | p_{1corr} > \\
&+ \delta(n'_1, n_1)\delta(n'_2, n_2)\delta(n'_4, n_3) < n'_{3corr} | \tau_{\pm} \sigma_{-\mu} | p_{1corr} > \\
&- \delta(n'_1, n_1)\delta(n'_2, n_2)\delta(n'_3, n_3) < n'_{4corr} | \tau_{\pm} \sigma_{-\mu} | p_{1corr} > .
\end{aligned} \tag{28}
$$

The anti-symmetrization of quasi-particles was considered for each of these amplitudes.

$$
\begin{aligned}
&p'_4 > p'_3 > p'_2 > p'_1; n'_4 > n'_3 > n'_2 > n'_1; \\
&p_4 > p_3 > p_2 > p_1; n_4 > n_3 > n_2 > n_1.
\end{aligned}
$$

The GT transitions were considered for the excited state of each phonon. The quasiparticle in the parent nucleus was assumed to be occupy the same orbit as the excited phonon. Further details of the formalism may be seen from Ref. [56].

The β decay partial half lives to daughter states Ψ were calculated using

$$
t_{\Psi} = \frac{K}{f_V(Z,E,A)B_F(\Psi) + (g_V/g_A)^{-2} f_A(Z,E,A)B_{\rm GT}(\Psi)}, \tag{29}
$$

where $E = (Q - \Psi)$, $g_A/g_V = -1.254$ [57], and $K = 6143$ s [58]. $f_A(Z,A,E)$ and $f_V(Z,A,E)$ are the integrals of the available phase space for axial vector and vector transitions, respectively. The phase space integrals were computed as per the recipe provided in Ref. [59]. The reduced transition probabilities for GT and Fermi transitions are denoted by B_{GT} and B_F, respectively. The details of the calculation of nuclear matrix elements have been reported in Ref. [60]. The total β decay half-lives were computed by including all transition probabilities to the daughter states within the Q window and summing the partial half-lives in the inverse relation

$$
T_{1/2} = \left(\sum_{0 \le \Psi \le Q} \left(\frac{1}{t_{\Psi}} \right) \right)^{-1}. \tag{30}
$$

The γ-heating rates, in stellar matter, were computed using

$$
\lambda_{\gamma} = \sum_{ij} P_i E_j \lambda_{ij}, \tag{31}
$$

where P_i represents the occupation probability of the i^{th} parent state, E_j represent the daughter energy levels, and λ_{ij} represents the sum of electron capture (EC) and positron decay (PD) rates for transitions from the parent state i to daughter level j

$$
\lambda_{ij} = K \left[f_{ij}^{\rm EC} + f_{ij}^{\rm PD} \right] \left[B(F_{ij}) + \left(\frac{g_A}{g_V} \right)^2 B({\rm GT}_{ij}) \right]. \tag{32}
$$

The first parenthesis on the right side of Eq. 32 are the phase-space integrals dependent on stellar temperature, density, and electron Fermi energy. These were computed using (in natural units)

$$
f_{ij}^{\rm PD} = \int_1^{\Psi_m} \Psi \sqrt{\Psi^2 - 1} (\Psi_m - \Psi)^3 F(-Z, \Psi)(1 - D_+) {\rm d}\Psi, \tag{33}
$$

$$
f_{ij}^{\rm EC} = \int_{\Psi_l}^{\infty} \Psi \sqrt{\Psi^2 - 1} (\Psi_m + \Psi)^3 F(Z, \Psi) D_- {\rm d}\Psi, \tag{34}
$$

where Ψ represents the electron or positron energy, Ψ_m is the available total β-decay energy, and Ψ_l represents the capture threshold energy. $F(\pm Z, \Psi)$ are the Fermi functions and $D_{\pm}$ represent the lepton distribution functions. For further details, refer to Ref. [61].

III. RESULTS AND DISCUSSION

This study investigates the effect of nuclear shape and pairing gaps on calculated γ-heating rates in the astrophysical environment. Our ensemble includes top 100 EC nuclei, which cover the range of A = 48−87 and Z = 21−36, and are based on the recent rankings published by Nabi *et al*. [49]. We employed four distinct pairing gaps: $\Delta^{(4)}$, $\Delta^{(5)}$, $\Delta^{(\rm LN)}$, and $\Delta^{(\rm MN)}$ and three nuclear deformation parameter sets derived from the β_2 [FRLDM (1981)], β_2 [FRDM (1992)], and β_2 [FRDM (2012)].

Figure 1 presents the calculated ground-state Gamow–Teller (GT) strength functions for ^{51}Cr, ^{56}Ni, ^{57}Co, and ^{64}Cu examined using the pn-QRPA framework by employing the selected sets of nuclear deformation and pairing gap values. The GT strength distributions calculated using our model are compared with the available experimental data [62]. The comparison provides an opportunity to gauge the performance of our selected nuclear model. Figure 1 reflects the sensitivity of transition strengths to both pairing correlations and quadrupole deformations. The abscissa shows daughter excitation energies up to the Q-values. The experimental data [62] were reported up to 0.75240, 2.13290, 0.83232, and 1.67460 MeV for ^{51}Cr, ^{56}Ni, ^{57}Co, and ^{64}Cu, respectively.

The measured data for ^{51}Cr exhibit two low-lying GT transitions at the ground state and at $E_x \approx 0.32$ MeV, indicating a simple single-particle configuration consistent with the odd-proton character of ^{51}Cr in the lower-fp

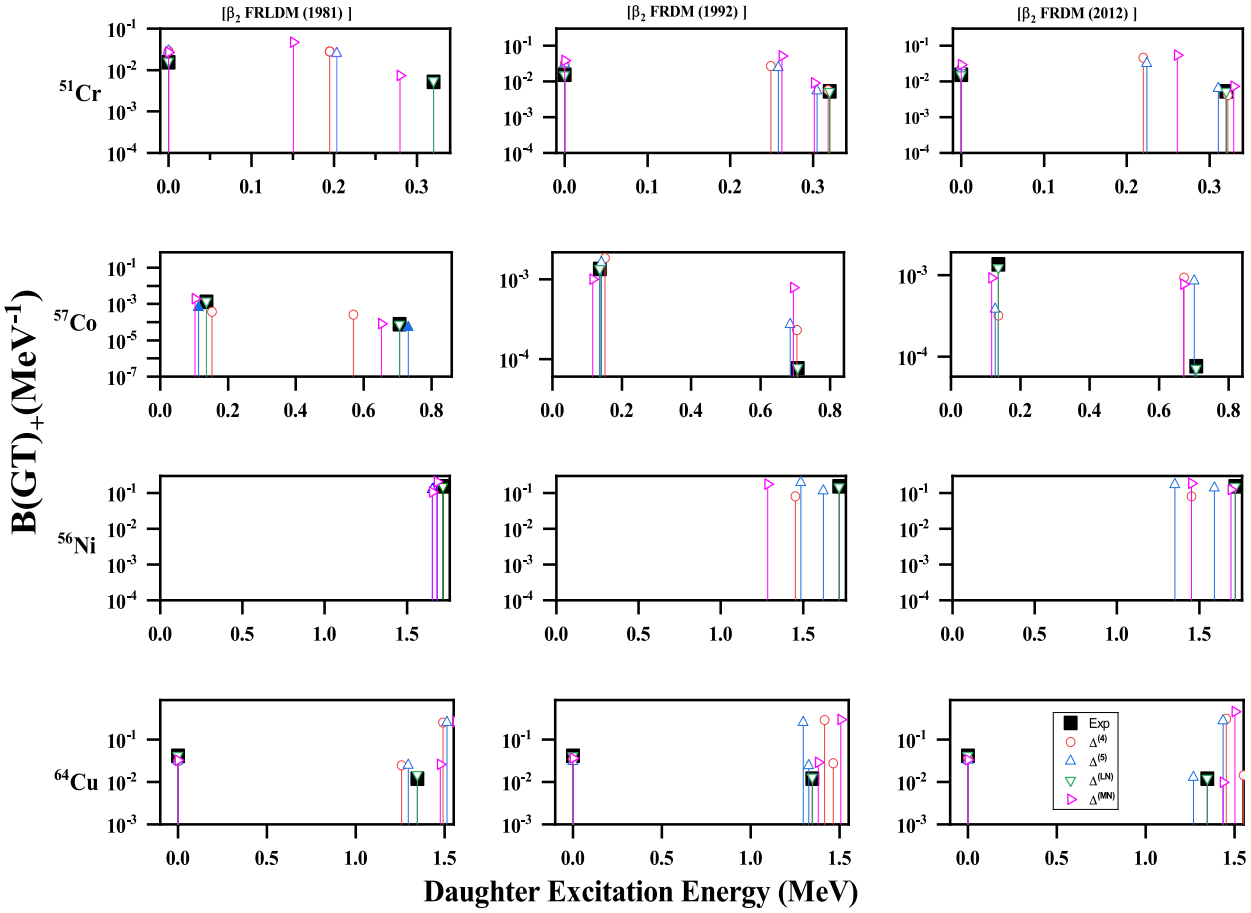

Fig. 1. (color online) Comparison of ground-state GT strength distributions for ^{51}Cr, ^{56}Ni, ^{57}Co, and ^{64}Cu using three distinct nuclear deformation values and four different pairing gap schemes with experimental data [62].

shell. The pn-QRPA calculations successfully reproduced the two GT transitions. The $\Delta^{(LN)}$ model provided the best agreement with experimental values, with $B(\mathrm{GT}) = 1.633\times10^{-2}$ MeV^{-1} and 5.52×10^{-3} MeV^{-1}. The improved correspondence results from the Lipkin–Nogami particle-number projection [50], which stabilizes pairing correlations and reduces artificial level fluctuations. The $\Delta^{(MN)}$ prescription enhanced the overall transition strength ($B(\mathrm{GT}) = 2.68\times10^{-2}$ MeV^{-1} and 7.27×10^{-3} MeV^{-1}), which is consistent with the stronger mass-scaled pairing field introduced by Madland and Nix [51]. The FRDM (1992) deformation resulted in a higher magnitude of GT strengths. The FRDM (2012) deformation, which incorporates updated microscopic corrections, produced the most balanced results. Experimentally, ^{56}Ni exhibits a prominent GT transition centered at $E_x \approx 1.72$ MeV with a strength of $B(\mathrm{GT}) = 1.5177\times10^{-1}$ MeV^{-1}. This strong, low-lying transition reflects a doubly magic, closed-shell configuration ($Z = N = 28$). The overall fragmentation pattern is minimal, consistent with the low collectivity expected for a near spherical nucleus. Our model reproduced the strong single GT transition reasonably well; however, small quantitative differences appear because of the sensitivity of closed-shell nuclei to the choice of pairing and deformation parameters. ^{57}Co exhibits two low-lying GT transitions around $E_x \approx 0.14$ MeV and 0.71 MeV, with corresponding B(GT) strengths of 1.35×10^{-3} MeV^{-1} and 7.606×10^{-5} MeV^{-1}, respectively. These weak transitions are consistent with the odd-proton configuration of ^{57}Co. The pn-QRPA results were comparable with the measured data. The odd-odd nucleus ^{64}Cu displays two dominant GT transitions: ground state and at $E_x \approx 1.35$ MeV. The significant ground-state component and moderately strong excited transition indicate a mixture of single-particle and weakly collective GT configurations, consistent with the odd–odd nature of ^{64}Cu. The pn-QRPA results reproduce these two transitions fairly well for all input parameters. The combination of FRDM (2012) deformation values and $\Delta^{(LN)}$ pairing gaps provided the closest agreement with measured data for the four selected nuclei.

The main feature of the current study is a comprehensive analysis of γ-heating rates attributed to the electron capture processes in astrophysical environments. Figs. 2–7 examine the sensitivity of these rates to nuclear

pairing gaps and ground-state deformations. Our calculations span the temperature range of 1−10 GK and density range of 10^9-10^{11} g/cm^3. We compare our calculated results with available shell model (SM) γ-ray heating rates [63], as presented in Figs. 2−7. The authors of Ref. [63] highlighted the critical issue of electron chemical potential and Q-values in the electron-capture transitions of fp-shell nuclei, and they incorporated electron screening effects in their calculations of electron-capture rates. Screening increases the electron fraction while simultaneously lowering the capture rates. In Ref. [63], the authors adopted the electron-capture rates for fp-shell nuclei from Honma *et al*. [64], while for other nuclei, they employed the rates reported in Refs. [41, 65, 66].

The empirical pairing gaps $\Delta^{(4)}$ and $\Delta^{(5)}$ predict comparable γ-heating rates (within a factor of 2–3), with $\Delta^{(5)}$ resulting in slightly enhanced rates at $T \geq 10$ GK. This similarity reflects their common theoretical foundation in finite-difference approximations of the pairing gap, with the $\Delta^{(5)}$ method providing a modest improvement through reduced sensitivity to single-level fluctuations. In contrast, the $\Delta^{(LN)}$ approach demonstrates markedly different behavior. The $\Delta^{(LN)}$ predicted γ-heating rates are around an order of magnitude smaller than those predicted by the empirical pairing gaps. This suppression can be attributed to the treatment of particle-number conservation and inclusion of higher-order correlations in this method, which significantly alter the predicted phase space for electron capture transitions. The $\Delta^{(MN)}$ model frequently resulted in intermediate values of γ-heating rates, between the finite-difference methods and Lipkin–Nogami approach.

For the majority of nuclei, under low-temperature and low-density conditions ($T = 1$ GK, $\rho = 10^7$ g/cm^3), the γ-heating rates are negligible ($\sim 10^{-40}-10^{-10}$ MeV·s^{-1}). Under these physical conditions, the excited states are not sufficiently populated, and electron capture proceeds from the parent ground state, resulting in low-energy transitions or stable daughter nuclei, yielding slight γ-ray heating.

On the other extreme, for selected high-temperature and high-density regions ($T = 10$ GK, $\rho = 10^{11}$ g/cm^3), the electron chemical potentials exceed typical nuclear Q-values. Under such extreme conditions, the sensitivity of γ-heating rates to pairing gaps diminishes considerably. The increased phase space for electron capture overwhelms subtle differences in the nuclear structure, resulting in the convergence of predictions across varying pairing gaps. All models converge to similar magnitudes $\sim (10^4-10^5)$ MeV·s^{-1}, suggesting reduced sensitivity to

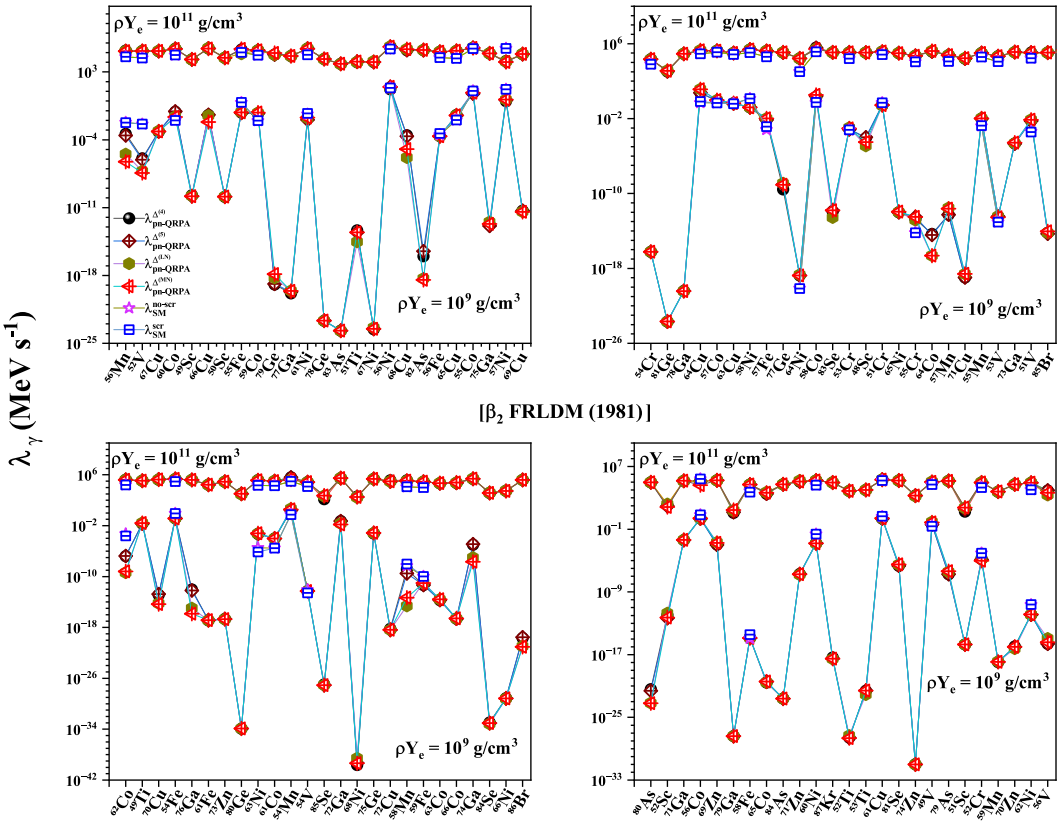

Fig. 2. (color online) pn-QRPA calculated γ -heating rates (MeV·s^{-1}) for the top 100 EC nuclei at $T = 1$ GK calculated using four different pairing gaps and β_2 [FRLDM (1981)] as input parameters. The shell model rates with and without screening effects are also shown [63].

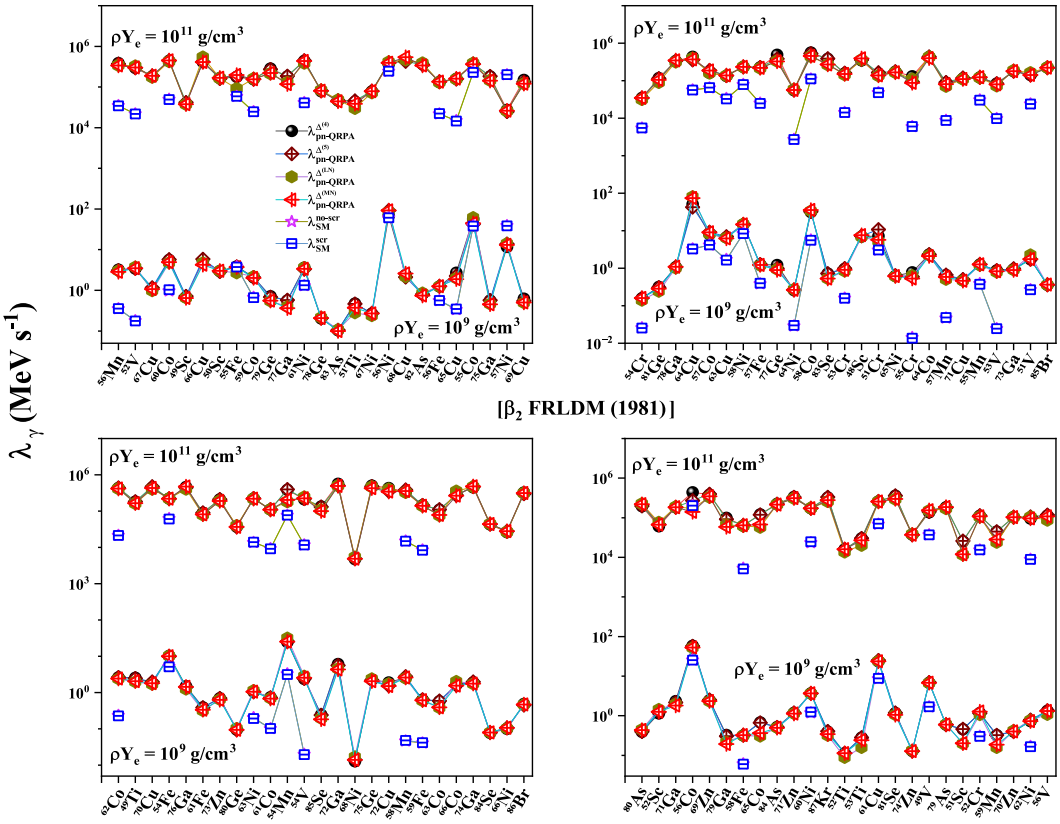

Fig. 3. (color online) Same as Fig. 2, at $T = 10$ GK.

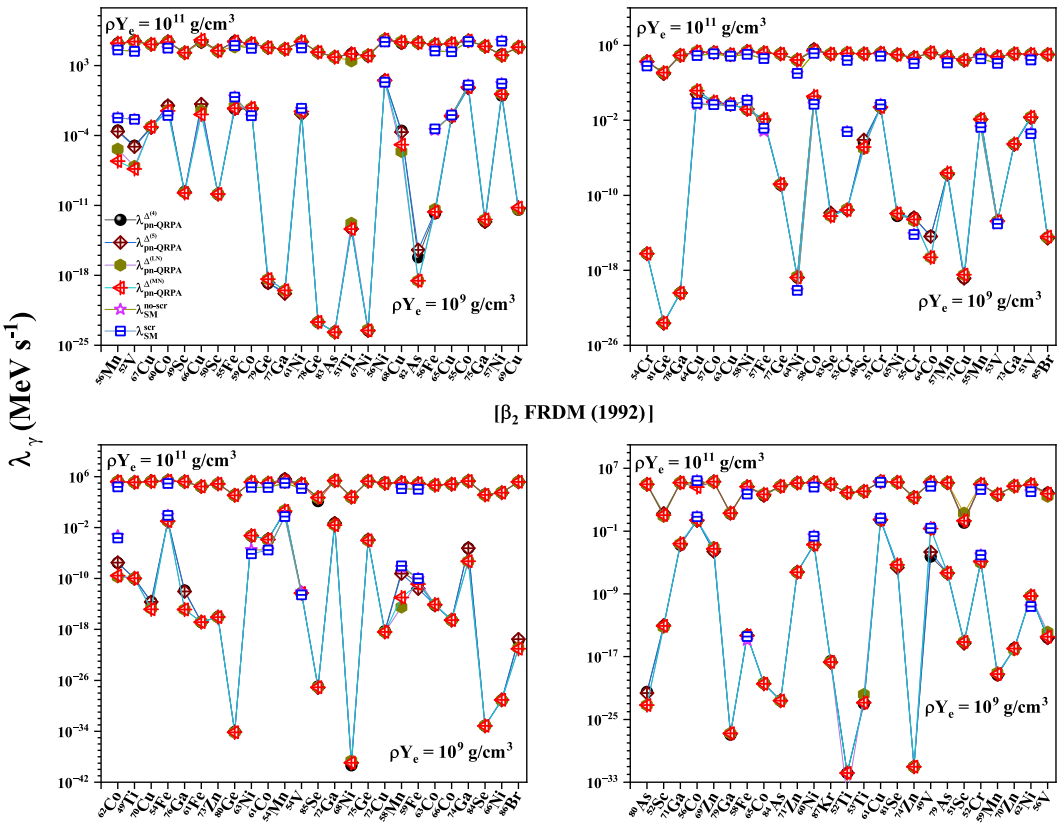

Fig. 4. (color online) Same as Fig. 2 ($T = 1$ GK), using β_2 [FRDM (1992)] as input parameter in the pn-QRPA rates.

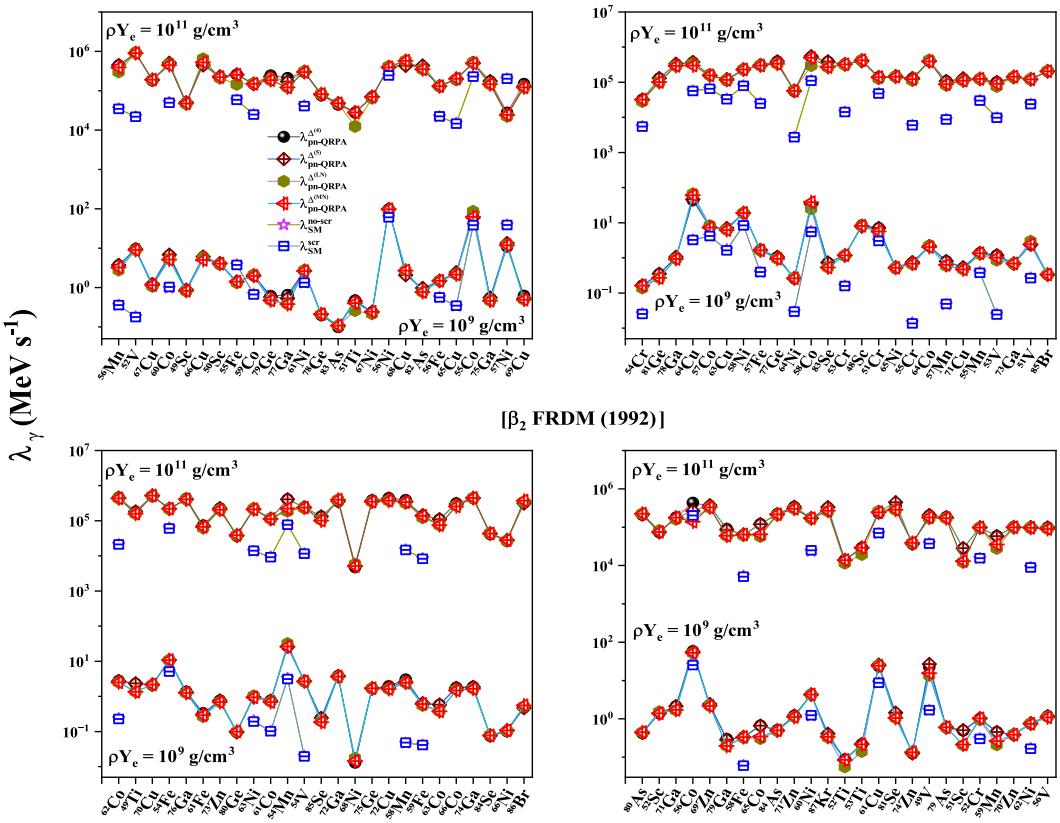

Fig. 5. (color online) Same as Fig. 4, at $T = 10$ GK.

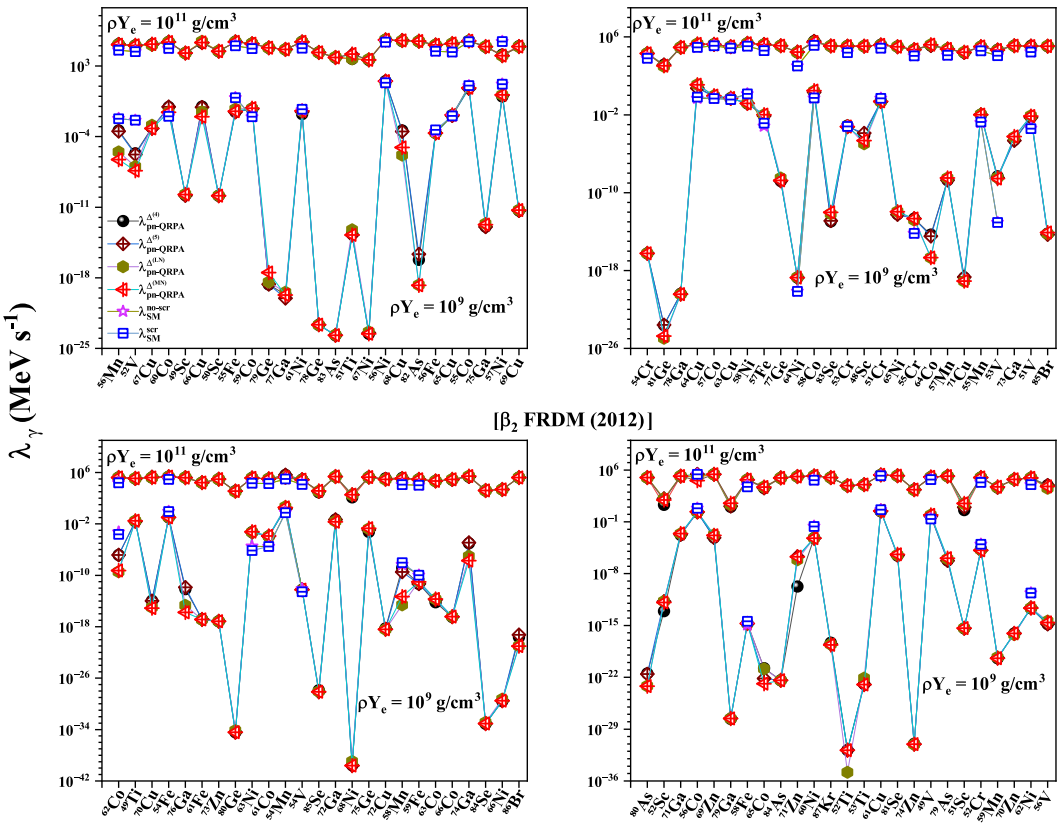

Fig. 6. (color online) Same as Fig. 2 ($T = 1$ GK), using β_2 [FRDM (2012)] as the input parameter in the pn-QRPA rates.

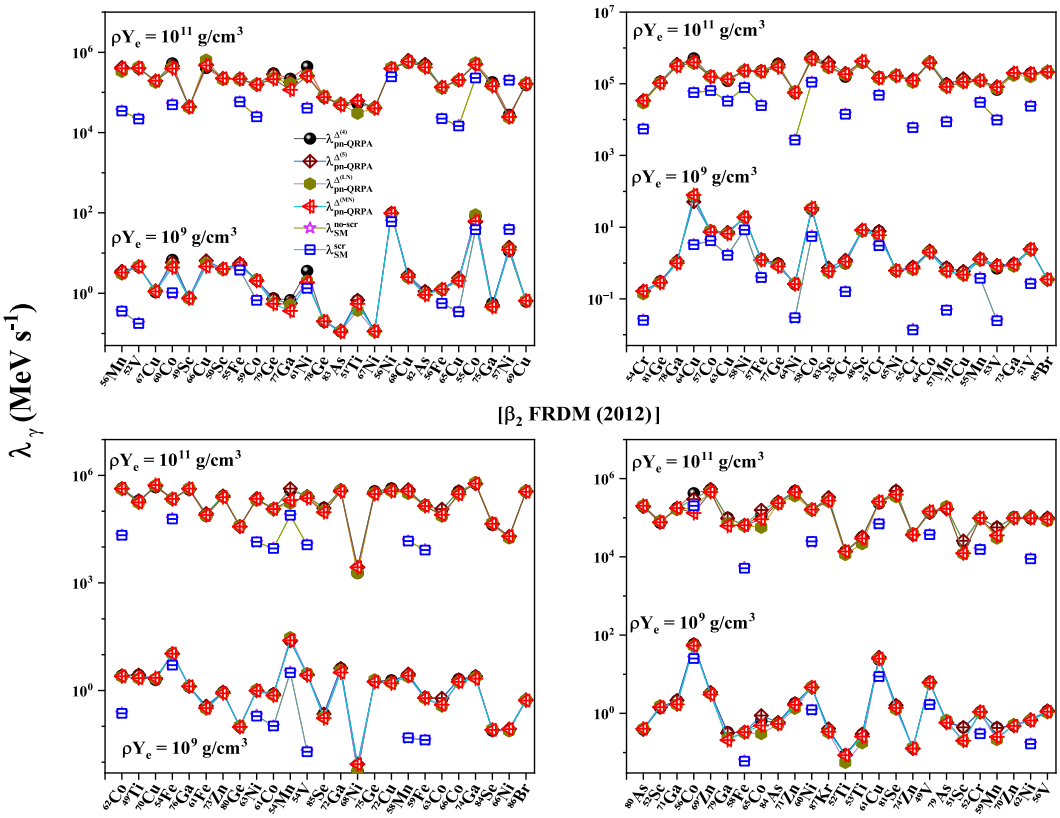

Fig. 7. (color online) Same as Fig. 6, at $T = 10$ GK.

pairing treatment under extreme conditions where thermal effects dominate.

The progression from β_2 [FRLDM (1981)] to β_2 [FRDM (1992)], and finally to β_2 [FRDM (2012)] affects γ-ray heating rate predictions because of substantial theoretical improvements in the treatment of nuclear deformations for neutron-rich nuclei and those with soft potential energy surfaces. The FRDM (2012) model incorporates a more sophisticated description of deformation energy surfaces and includes a density-symmetry coefficient L set to zero. These improvements affect nuclei with soft potential energy surfaces, where small changes in the deformation energy landscape can alter the predicted ground-state deformations. For a realistic simulation of superbursts and post-silicon burning phases of stars, the FRDM (2012) deformation parameters should be employed with $\Delta^{(LN)}$ pairing gaps because they can provide the best prediction power to our nuclear model.

Tables 1–2 list the ratio of pn-QRPA calculated mean γ-heating rates to those obtained from SM calculations [63]. The ratios are presented for pn-QRPA rates using different choices of pairing gaps and nuclear deformations. Table 1 lists the computed ratio with SM calculations excluding screening effects. At high temperatures, the pn-QRPA rates are larger than the SM rates by an order of magnitude. At $T = (1–3)$ GK and $\rho Y_e = 10^{11}$ g/cm^3, the pn-QRPA rates are larger than the SM rates by a factor of 4–5. Table 2 indicates that the screening effects in the SM calculation are the highest at low temperature ($T = 1$ GK) and low density ($\rho Y_e = 10^9$ g/cm^3), where the SM rates reduce up to a factor of 2.6. Under such physical conditions, the pn-QRPA rates are larger than the corresponding SM rates by up to a factor of 25. The comparison at higher density ($\rho Y_e = 10^{11}$ g/cm^3) is similar to that exhibited in Table 1.

We wanted to identify the maximum change in the calculated γ-heating rates as a result of changing pairing gaps and nuclear deformation values. For computed γ-heating rates bearing negative exponents, orders of magnitude changes can be attributed to a small variation in model input parameters; however, they are not of any significance in simulation studies because of their almost zero impact. Fig. 8 shows computed γ-heating rates at a density of 10^9 g/cm^3 and $T = 1$ GK. These conditions correspond to the physical environment of superbursts in accreting neutron stars [4]. The spread in γ-heating rates is obtained by varying the nuclear deformation parameter β_2 and different prescriptions for pairing gaps, which highlights the sensitivity of weak-interaction rates to nuclear structure inputs. From a physical perspective, nuclear deformation modifies single-particle level densities and transition strengths, while pairing correlations alter the availability of quasiparticle states. These effects directly affect the electron-capture chains and associated γ-emis-

Table 1. Comparison of the reported pn-QRPA calculated mean γ -heating rates with shell model rates excluding screening effects [63].

T(GK)	$\bar{\lambda}^{\Delta^{(4)}}_{\rm pnQRPA}/\bar{\lambda}^{\rm no-scr}_{\rm SM}$	$\bar{\lambda}^{\Delta^{(5)}}_{\rm pnQRPA}/\bar{\lambda}^{\rm no-scr}_{\rm SM}$	$\bar{\lambda}^{\Delta^{(LN)}}_{\rm pnQRPA}/\bar{\lambda}^{\rm no-scr}_{\rm SM}$	$\bar{\lambda}^{\Delta^{(MN)}}_{\rm pnQRPA}/\bar{\lambda}^{\rm no-scr}_{\rm SM}$	$\bar{\lambda}^{\Delta^{(4)}}_{\rm pnQRPA}/\bar{\lambda}^{\rm no-scr}_{\rm SM}$	$\bar{\lambda}^{\Delta^{(5)}}_{\rm pnQRPA}/\bar{\lambda}^{\rm no-scr}_{\rm SM}$	$\bar{\lambda}^{\Delta^{(LN)}}_{\rm pnQRPA}/\bar{\lambda}^{\rm no-scr}_{\rm SM}$	$\bar{\lambda}^{\Delta^{(MN)}}_{\rm pnQRPA}/\bar{\lambda}^{\rm no-scr}_{\rm SM}$
	β_2 [FRLDM (1981)]							
	$\rho Y_e = 10^9$ g/cm^3				$\rho Y_e = 10^{11}$ g/cm^3			
1	7.86	8.16	8.75	9.76	4.44	4.38	4.20	4.31
3	6.39	6.57	7.37	7.22	4.63	4.61	4.46	4.59
10	11.56	11.38	11.87	11.33	8.76	8.71	8.41	8.42
	β_2 [FRDM (1992)]							
1	10.41	10.23	10.73	10.94	4.61	4.63	4.39	4.49
3	6.30	6.33	6.97	6.83	5.31	5.31	5.05	5.18
10	13.74	13.65	12.65	12.87	10.07	10.08	9.33	9.62
	β_2 [FRDM (2012)]							
1	8.29	8.08	9.00	9.40	4.45	4.41	4.24	4.30
3	6.99	7.00	7.73	7.39	4.82	4.80	4.64	4.72
10	12.42	12.67	12.23	12.05	9.14	9.28	8.64	8.83

Table 2. Comparison of the reported pn-QRPA calculated mean γ -heating rates with shell model rates including screening effects [63].

T(GK)	$\bar{\lambda}^{\Delta^{(4)}}_{\rm pnQRPA}/\bar{\lambda}^{\rm scr}_{\rm SM}$	$\bar{\lambda}^{\Delta^{(5)}}_{\rm pnQRPA}/\bar{\lambda}^{\rm scr}_{\rm SM}$	$\bar{\lambda}^{\Delta^{(LN)}}_{\rm pnQRPA}/\bar{\lambda}^{\rm scr}_{\rm SM}$	$\bar{\lambda}^{\Delta^{(MN)}}_{\rm pnQRPA}/\bar{\lambda}^{\rm scr}_{\rm SM}$	$\bar{\lambda}^{\Delta^{(4)}}_{\rm pnQRPA}/\bar{\lambda}^{\rm scr}_{\rm SM}$	$\bar{\lambda}^{\Delta^{(5)}}_{\rm pnQRPA}/\bar{\lambda}^{\rm scr}_{\rm SM}$	$\bar{\lambda}^{\Delta^{(LN)}}_{\rm pnQRPA}/\bar{\lambda}^{\rm scr}_{\rm SM}$	$\bar{\lambda}^{\Delta^{(MN)}}_{\rm pnQRPA}/\bar{\lambda}^{\rm scr}_{\rm SM}$
	β_2 [FRLDM (1981)]							
	$\rho Y_e = 10^9$ g/cm^3				$\rho Y_e = 10^{11}$ g/cm^3			
1	20.8	20.2	22.1	25.1	4.51	4.44	4.27	4.37
3	6.94	7.17	7.90	7.83	4.69	4.67	4.52	4.65
10	11.6	11.4	11.9	11.3	8.76	8.71	8.41	8.42
	β_2 [FRDM (1992)]							
1	23.2	22.4	24.1	25.0	4.68	4.69	4.45	4.56
3	6.88	6.92	7.53	7.39	5.37	5.36	5.11	5.24
10	13.8	13.7	12.7	12.9	10.1	10.1	9.33	9.61
	β_2 [FRDM (2012)]							
1	21.1	20.6	22.5	24.0	4.52	4.47	4.30	4.36
3	7.69	7.73	8.41	8.07	4.88	4.86	4.70	4.78
10	12.4	12.7	12.3	12.1	9.13	9.27	8.64	8.83

sion, which are key contributors to crustal heating.

For a more meaningful analysis, Fig. 9 displays the top three cases where the maximum change of heating rate occurs for nuclei possessing γ-heating rates of magnitude that are larger than 1 MeV·s^{-1}. Fig. 9 illustrates the maximum change in the calculated γ-heating rates as a result of changing either the pairing gaps or deformation values. Fig. 9 also shows that changing β_2 values result in a larger effect on computed heating rates compared to that achieved using changing pairing gaps. The γ-heating rates change up to a factor of 26 and 16 by changing the deformation and pairing gap values, respectively. The left panel of Fig. 9 shows the maximum variation in computed heating rates when we alter the pairing gaps in our nuclear model. For ^{51}Sc, a change in γ-heating rates by a factor of 16 was noted at $T = 1$ GK, $\rho = 10^{11}$ g/cm^3. For the remaining two nuclei, ^{51}Ti ($T = 1$ GK, $\rho = 10^{11}$ g/cm^3) and ^{56}Co ($T = 3$ GK, $\rho = 10^{11}$ g/cm^3), the heating rate changed by a factor of 4–5. The right panel displays the maximum change in computed γ-heating rates when

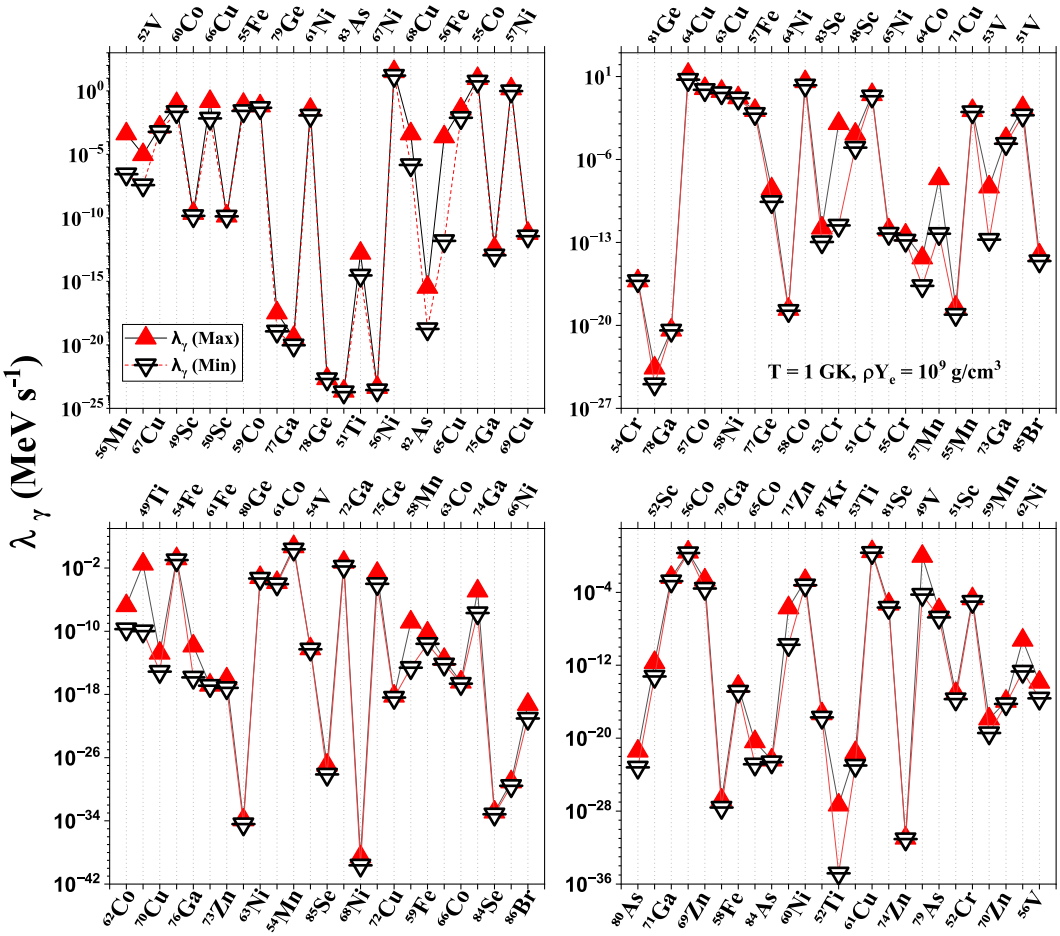

Fig. 8. (color online) Maximum and minimum calculated γ-ray heating rates (MeV·s $^{-1}$) by changing pairing gaps and deformations for the top 100 EC nuclei under superburst conditions.

we vary the β_2 values. The maximum change by a factor of 26 was noted for ^{51}Sc ($T = 1$ GK, $\rho = 10^{11}$ g/cm^3). The heating rates changed by more than an order of magnitude, and it was observed for ^{49}V ($T = 10$ GK, $\rho = 10^9$ g/cm^3) and ^{52}Sc ($T = 1$ GK, $\rho = 10^{11}$ g/cm^3) because of the changing β_2 values. A more refined inspection reveals that the calculated γ-heating rates are a sensitive function of the pairing gaps and deformations when a nucleus approaches a magic proton, magic neutron, or a magic mass number. Near these shell closures, nuclei tend to favor spherical configurations, and even a minute departure of β_2 from zero can induce substantial modifications in the predicted heating rates. The intensity of the pairing interaction within a nucleus is governed by residual pairing correlations and the density of single-particle levels near the Fermi surface. As nuclei near magic numbers undergo structural rearrangements in their Fermi surfaces, alterations in the pairing gaps can exert a pronounced influence on the resulting γ-heating rates.

Figure 10 presents the calculated γ-heating rates averaged over the selected 100 nuclei and presented as snapshots of predetermined temperature and density values. For stellar temperatures [$T = (1–3)$ GK], the heating rates remain minimal, typically in the range of 10^{-5}–10^{-4} MeV·s^{-1} at a low density of 10^7 g·cm^{-3}. At $T = 10$ GK and density ($\rho Y_e = 10^{11}$ g·cm^{-3}), the rates increase by several orders of magnitude, reaching values in the range of (10^4–10^5) MeV·s^{-1}. This enhancement is attributed to the growing contribution of thermally populated excited states. At a given temperature, γ-ray heating rates increase monotonically with density. High-density environments increase the Fermi energy values (up to 24 MeV) enhancing electron captures to excited states by orders of magnitude and subsequent γ-emissions. β_2 [FRLDM (1981)] resulted in comparatively lower heating rates at temperatures [$T = (1–3)$ GK] followed by β_2 [FRDM (1992)] rates. β_2 [FRDM (2012)] provided the highest γ-heating rates, highlighting the revised microscopic corrections that resulted in enhanced transition rates. Pairing gap variations affect the predicted heating rates to a lesser extent. For temperatures around 10 GK, and for all density regions covered in the current investigation, the highest average heating rate of $\bar{\lambda}_\gamma = 2.27\times10^5$ MeV·s^{-1} resulted from the $\Delta^{(4)}/\Delta^{(5)}$ pairing gap formula and

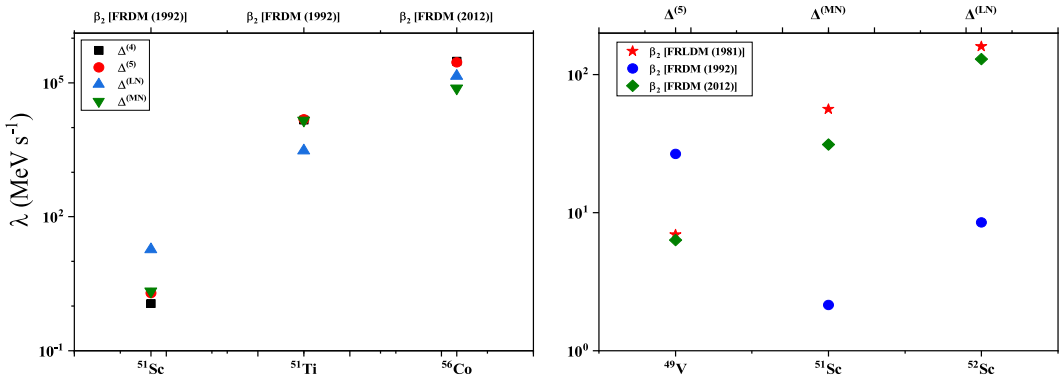

Fig. 9. (color online) Top three variations in the calculated γ-heating rates of magnitude bigger than 1 MeV·s^{-1} with changing input parameters. The physical conditions are presented in the text.

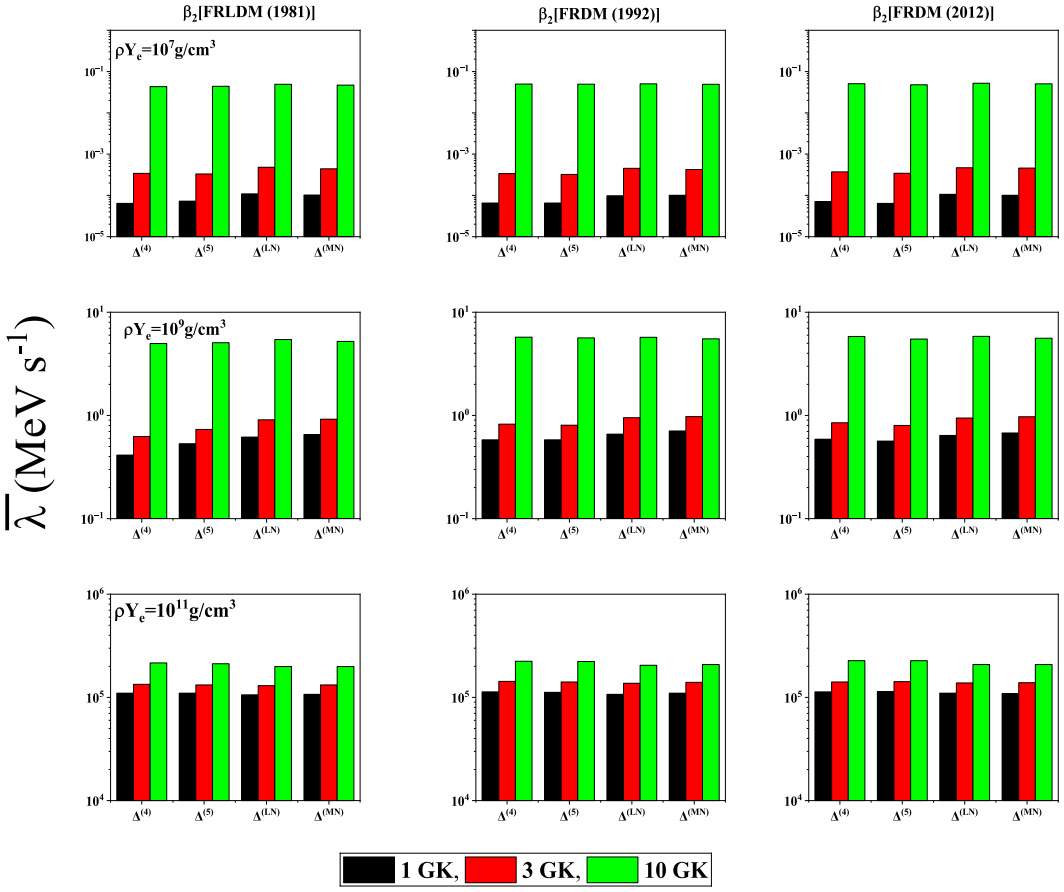

Fig. 10. (color online) Comparison of the calculated γ-ray heating rates (MeV·s^{-1}) averaged over the selected top 100 EC nuclei, as a function of pairing gaps and deformations.

FRDM (2012) nuclear deformation parameters. Under superburst ignition conditions, our nuclear model predicted maximum and minimum mean γ-heating rates of $\bar{\lambda}_\gamma = 7.08\times10^{-1}$ MeV s^{-1} and $\bar{\lambda}_\gamma = 4.13\times10^{-1}$ MeV·s^{-1}, respectively, for the top 100 EC nuclei selected in our investigation. The maximum mean heating rates were predicted using the $\Delta^{(MN)}$ pairing gap and nuclear deformation parameters from the FRDM (1992) model. The minimum γ-heating rates were determined by employing the $\Delta^{(4)}$ pairing gap and β_2 values from the FRLDM (1981) model.

IV. CONCLUSIONS

In this study, we presented calculations of the γ-heating rates attributed to weak interaction decays in stellar matter. Our pool of nuclei consisted of top 100 EC nuclei possessing astrophysical importance. These nuclei were

selected based on their respective contribution to the time rate of change of the lepton fraction ($\dot{Y}_e$) during presupernova evolution, as identified in a recent simulation study [49]. A key feature of our computation was the microscopic calculation of GT strength distributions for both ground and excited states. Pairing gaps and nuclear deformations serve as essential model parameters for calculating the properties of the nuclear structure. The current investigation highlighted that changing pairing gaps and nuclear deformation values influenced the GT strength distributions and associated γ-heating energy rates. For low-density and low-temperature regions, the lowest mean heating rate of $\bar{\lambda}_\gamma = 6.39\times10^{-5}$ MeV·s^{-1} was recorded for $\Delta^{(4)}$ pairing gaps and FRLDM (1981) nuclear deformations. For high-density and high-temperature zones, the highest mean heating rate of $\bar{\lambda}_\gamma = 2.27\times10^{5}$ MeV·s^{-1} was computed for $\Delta^{(4)}/\Delta^{(5)}$ pairing gaps and FRDM (2012) nuclear deformations. The calculated γ-heating rates changed by up to a factor 26 through a change in deformation values. Altering pairing gaps changed the heating rates up to a factor of 16. These changes bear significance in reducing the ignition depths of superbursts and counteracting the reduction in crust temperature resulting from Cooper pair neutrino emissions. Our results suggest that nuclear structure properties can significantly alter the intensity of crustal heating. The interplay between pairing gap prescriptions and deformation parameters can shape the microscopic heating profiles and thermal evolution of accreting neutron star crusts.

References

[1] H. A. Bethe, Phys. Rev. **55**, 434 (1939)
[2] E. M. Burbidge, G. R. Burbidge, W. A. Fowler *et al.*, Rev. Mod. Phys. **29**, 547 (1957)
[3] W. Baade and F. Zwicky, Proc. Natl. Acad. Sci. USA **20**, 259 (1934)
[4] A. Cumming, J. Macbeth, and D. Page, Astrophys. J. **646**, 429 (2006)
[5] E. Flowers, M. Ruderman, and P. Sutherland, Astrophys. J. **205**, 541 (1976)
[6] S. Gupta, E. F. Brown, H. Schatz *et al.*, Astrophys. J. **662**, 1188 (2007)
[7] H. A. Bethe, G. E. Brown, J. Applegate *et al.*, Nucl. Phys. A **324**, 487 (1979)
[8] S. Usman and A. Mushtaq, Sci. Rep. **13**, 15315 (2023)
[9] H.T. Janka, K. Langanke, A. Marek *et al.*, Phys. Rep. **442**, 38 (2007)
[10] B. Pritychenko, M. Birch, B. Singh *et al.*, At. Data Nucl. Data Tables **107**, 1 (2016)
[11] N. J. Stone, At. Data Nucl. Data Tables **111**, 1 (2016)
[12] K. Zhang, M. K. Cheoun, Y. B. Choi *et al.*, At. Data Nucl. Data Tables **144**, 101488 (2022)
[13] P. Guo, X. Cao, K. Chen *et al.*, At. Data Nucl. Data Tables **158**, 101661 (2024)
[14] M. Bender, P.-H. Heenen, and P.-G. Reinhard, Rev. Mod. Phys. **75**, 121 (2003)
[15] J. M. Lattimer, K. A. van Riper, M. Prakash *et al.*, Astrophys. J. **425**, 802 (1994)
[16] D. Page and S. Reddy, in *Neutron Star Crust*, edited by C. A. Bertulani and J. Piekarewicz (Hauppauge, N.Y.: Nova Publishers, 2012), p. 281
[17] J. Piekarewicz, F. J. Fattoyev, and C. J. Horowitz, Phys. Rev. C **90**, 015803 (2014)
[18] X. Shang and A. Li, Astrophys. J. **923**, 108 (2021)
[19] U. Lombardo, H. Schulze, C. W. Shen *et al.*, Int. J. Mod. Phys. E **14**, 513 (2005)
[20] H. Wibowo, E. Litvinova, Y. Zhang *et al.*, Phys. Rev. C **102**, 054321 (2020)
[21] E. Yüksel, Nucl. Phys. A **1014**, 122238 (2021)
[22] R. Lisboa, M. Malheiro, and B. V. Carlson, Phys. Rev. C **93**, 024321 (2016)
[23] Y. F. Niu, Z. M. Niu, N. Paar *et al.*, Phys. Rev. C **88**, 034308 (2013)
[24] N. D. Dang and A. Arima, Phys. Rev. C **68**, 044303 (2003)
[25] Y. F. Niu, N. Paar, D. Vretenar *et al.*, Phys. Lett. B **681**, 315 (2009)
[26] E. Litvinova and P. Schuck, Phys. Rev. C **104**, 044330 (2021)
[27] H. Wibowo and E. Litvinova, Phys. Rev. C **106**, 044304 (2022)
[28] L. G. Moretto, Phys. Lett. B **40**, 1 (1972)
[29] N. D. Dang, P. Ring, and R. Rossignoli, Phys. Rev. C **47**, 606 (1993)
[30] V. Zelevinsky, B. A. Brown, N. Frazier *et al.*, Phys. Rep. **276**, 85 (1996)
[31] A. Volya, B. A. Brown, and V. Zelevinsky, Phys. Lett. B **509**, 37 (2001)
[32] A. Ravlić, E. Yüksel, T. Nikšić *et al.*, Nat. Commun. **14**, 4834 (2023)
[33] N. D. Dang, K. Tanabe, and A. Arima, Nucl. Phys. A **675**, 531 (2000)
[34] J.-U. Nabi and H. V. Klapdor-Kleingrothaus, Eur. Phys. J. A **5**, 337 (1999)
[35] A. A. Dzhioev, K. Langanke, G. Martínez-Pinedo *et al.*, Phys. Rev. C **101**, 025805 (2020)
[36] E. Yüksel, N. Paar, G. Colò *et al.*, Phys. Rev. C **101**, 044305 (2020)
[37] A. F. Fantina, E. Khan, G. Colò *et al.*, Phys. Rev. C **86**, 035805 (2012)
[38] E. Litvinova and C. Robin, Phys. Rev. C **103**, 024326 (2021)
[39] E. Yüksel, N. Paar, G. Colò *et al.*, Phys. Rev. C **101**, 044305 (2020)
[40] G. M. Fuller, W. A. Fowler, and M. J. Newman, Astrophys. J. Suppl. Ser. **42**, 447 (1980)
[41] G. M. Fuller, W. A. Fowler, and M. J. Newman, Astrophys. J. Suppl. Ser. **48**, 279 (1982)
[42] G. M. Fuller, W. A. Fowler, and M. J. Newman, Astrophys. J. **293**, 1 (1985)
[43] M. B. Aufderheide, I. Fushiki, S. E. Woosley *et al.*, Astrophys. J. Suppl. Ser. **91**, 389 (1994)
[44] K. Langanke and G. Martínez-Pinedo, Nucl. Phys. A **673**, 48 (2000)
[45] J. Pruet and G. M. Fuller, Astrophys. J. Suppl. Ser. **149**, 189 (2003)

[46] D. M. Brink, *The Influence of the Individual Nuclear Levels on the Widths of Nuclear Resonances*, Ph.D. thesis (Oxford: University of Oxford, 1955)
[47] P. Axel, Phys. Rev. **126**, 671 (1962)
[48] J.-U. Nabi, M. Nayab, and C. W. Johnson, J. Phys. G: Nucl. Part. Phys. **49**, 065201 (2022)
[49] J.-U. Nabi, A. Ullah, and A. A. Khan, Astrophys. J. **911**, 93 (2021)
[50] P. Möller, M. Mumpower, T. Kawano *et al*., At. Data Nucl. Data Tables **125**, 1 (2019)
[51] D. G. Madland and J. R. Nix, Nucl. Phys. A **476**, 1 (1988)
[52] S. A. Changizi, C. Qi, and R. Wyss, Nucl. Phys. A **940**, 210 (2015)
[53] P. Möller and J. R. Nix, At. Data Nucl. Data Tables **26**, 165 (1981)
[54] P. Möller, J. R. Nix, W. D. Myers *et al*., At. Data Nucl. Data Tables **59**, 185 (1995)
[55] P. Möller, A. J. Sierk, T. Ichikawa *et al*., At. Data Nucl. Data Tables **109**, 1 (2016)
[56] K. Muto, E. Bender and H. V. Klapdor, Z. Phys. A **333**, 125 (1989)
[57] K. Nakamura (Particle Data Group) *et al*, J. Phys. G **37**, 075021 (2010)
[58] J. C. Hardy and I. S. Towner, Phys. Rev. C **79**, 055502 (2009)
[59] N. B. Gove and M. J. Martin, At. Data Nucl. Data Tables **10**, 205 (1971)
[60] J.-U. Nabi, A. Ullah, and M. A. Qammar, Nucl. Phys. A **2025**, 123237 (2025)
[61] J.-U. Nabi and H. V. Klapdor-Kleingrothaus, At. Data Nucl. Data Tables **88**, 237 (2004)
[62] National Nuclear Data Center (NNDC), Brookhaven National Laboratory, https://www.nndc.bnl.gov/, retrieved 26th September 2025
[63] K. Mori, T. Suzuki, M. Honma *et al*., Astrophys. J. **904**, 29 (2020)
[64] M. Honma, T. Otsuka, T. Mizusaki *et al*., J. Phys.: Conf. Ser. **20**, 7 (2005)
[65] G. M. Fuller, W. A. Fowler, and M. J. Newman, Astrophys. J. **252**, 715 (1982)
[66] T. Oda, M. Hino, K. Muto *et al*., At. Data Nucl. Data Tables **56**, 231 (1994)